Scientific Research Publishing

International Journal of Astronomy and Astrophysics, 2023, 13, 172-194
https://www.scirp.org/journal/ijaa
ISSN Online: 2161-4725
ISSN Print: 2161-4717

The RXTE/PCA 35-Day X-Ray Lightcurve of Hercules X-1

Denis Leahy[1], Sandra Gonzalez Enriquez[2]

[1]Department of Physics and Astronomy, University of Calgary, Calgary, Canada
[2]Division de Ciencias e Ingenierias, Universidad de Guanajuato, Guanajuato, Mexico
Email: leahy@ucalgary.ca

How to cite this paper: Leahy, D. and Enriquez, S.G. (2023) The RXTE/PCA 35-Day X-Ray Lightcurve of Hercules X-1. *International Journal of Astronomy and Astrophysics*, **13**, 172-194.
https://doi.org/10.4236/ijaa.2023.133011

Received: July 3, 2023
Accepted: September 4, 2023
Published: September 7, 2023

Abstract

The archival Rossi X-ray Timing Explorer (RXTE) Proportional Counter Array (PCA) observations of HZ Her/Her X-1 are analyzed here. The time periods for Anomalous Low States are refined. The 35-day X-ray lightcurve of Her X-1 is produced using 35-day phases determined with RXTE All-Sky Monitor (ASM) and Swift Burst Alert Telescope (BAT) data, with adjustments based on the RXTE/PCA data. As a result, we constructed the best-phased 35-day lightcurve of Her X-1 with the highest sensitivity. The RXTE/PCA data are separated into 8 different substates of the 35-day cycle: Main High (MH) turn-on, MH, MH decline, Low State (LS) 1, Short High (SH) turn-on, SH, SH decline, and LS2. Orbital lightcurves are created for each substate, and they are compared. Eclipse data are extracted for each substate to determine the changes in eclipse shape with 35-day phase. A scattering corona model is fit to the eclipses for the different 35-day substates: this shows that the corona is present with similar intensity at all 35-day phases. We search for previously reported dips without absorption but find none.

Keywords

X-Ray Binaries, Light-Curves, Accretion Disks

1. Introduction

Hercules X-1 (Her X-1) is a well-known and studied binary system (e.g. [1] [2] [3]) consisting of the neutron star Her X-1—pulsating at 1.24 s—in a 1.7-day nearly circular orbit around its optical companion, a main sequence star HZ Her of spectral type A/F. The binary has accurately measured orbital ephemeris [4]. The companion varies between late A-type (for the back side facing away from the neutron star) and early B-type (for the front X-ray illuminated side of the

companion). The approximate masses of the neutron star and the companion are ≃1.6 $M_{\odot}$ and ≃2.3 $M_{\odot}$, respectively [5] [6]. The main uncertainty is caused by the uncertainty in the orbital inclination, which is ~85˚. It is located at a distance of ~6.1 kpc from Earth [5] (updated recently with Gaia to $5.0^{+0.6}_{-0.7}$ kpc [7]), with J2000 coordinates of RA = 16 57 49.830 and dec = +35 20 32.60, or Galactic coordinates of 58.1491˚ longitude and 37.5230˚ latitude. Her X-1 is a persistent X-ray pulsar discovered by the Uhuru satellite in 1972 along with Centaurus X-3. Since that date, both pulsars have remained among the most studied X-ray sources and continue to provide new insights into X-ray binary astrophysics. The system Her X-1/HZ Her is a strong emitter in X-rays, optical, and ultraviolet (e.g. [8] [9] [10]), which allows detailed studies of the binary.

The 35-day cycle is one of the most prominent features of Her X-1 ([11] and references therein). The cause of the 35-day cycle as changes in the obscuration of the neutron star by a precessing accretion disk was identified early [12]. The first mechanism proposed was the mass stream from a precessing companion star [12]. However, the correct mechanism of radiation driven precession was proposed much later [13]. The length of the cycle (35 days) was explained by the specific parameters of the Her X-1 system including disk viscosity, neutron star luminosity, outer disk radius and mass transfer radius. [13] proposed that feedback between the neutron star luminosity and accretion rate from the disk would cause non-periodic precession (variable cycle lengths). The precessing accretion disk model was verified by [14], and the disk properties were measured by [15]. The 35-day cycle length can vary from 33 to 37 days ([16]). Turn-on of the 35-day cycle is defined by the sharp rise in flux at start of the Main High state (see next paragraph), and was proposed to start only at orbital phases 0.23 and 0.68 by [17]. This implies the 35-day cycle is either an integer or half-integer number of binary orbits long, with the most common value of 20.5 orbits. Later work using better data ([16] [18] [19]) showed that the integer/half-integer of orbits per 35-day cycle was not accurate. An alternative explanation proposed by [20] is a precessing thick ring. The binary system is shown conceptually in **Figure 1**, with an observer inclination of ≃85˚ and with a twisted and tilted accretion disk fed by an accretion stream from the Roche-lobe filling companion, HZ Her. The neutron star is directly visible in the MH state, and seen partially obscured in the SH state.

The 35-day cycle has 8 substates: Main High (MH) turn-on, MH, MH decline, Low State (LS) 1, Short High (SH) turn-on, SH, SH decline, and LS 2. These are obtained by dividing MH and SH states into their 3 different parts, and distinguishing the two LS. The MH state (including the 3 subdivisions) lasts 10 - 12 days, the SH state lasts 5 - 7 days, and MH and SH are separated by LS lasting 8 - 10 days [17]. In addition, Her X-1 has Anomalous Low States (ALS) (e.g. [21]), where the high states do not occur and instead exhibit extended periods of low X-ray flux for several months. ALS have been observed in 1983, 1993, 1999 and 2004, with no ALS reported since 2004. The ALS were discovered by [22], and shown by [11] to be indistinguishable from the regular LS based on the X-ray

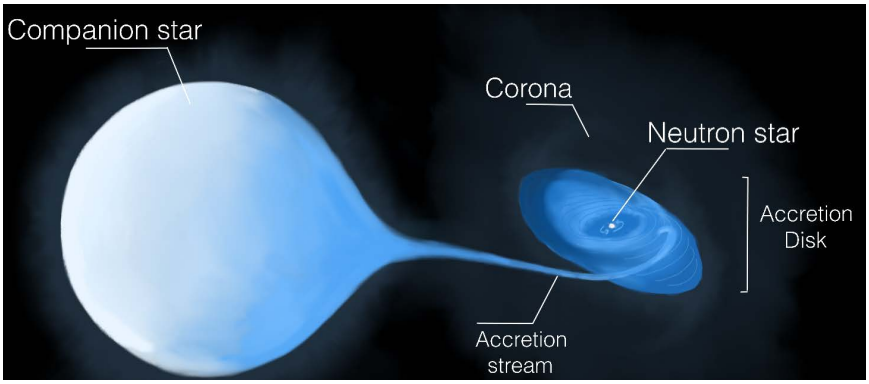

Figure 1. Conceptual diagram (artificial colors) of the binary system HZ Her/Her X-1 (companion star/neutron star) with its characteristic tilted and twisted accretion disk. The companion star is heated by the X-rays from the neutron star to ≃17,000 K for the heated side; the temperature is ≃8100 K for the unheated side. This causes the spectral type to vary with orbital phase.

softness ratio (SR). The ALS are likely produced by a change in the geometry of the accretion disk that prevents a direct line of sight to Her X-1 [23].

An X-ray binary system that has a low mass ($\lesssim 3\ M_{\odot}$) companion star is known as a low-mass X-ray binary (LMXB). The neutron star or black hole accretes material from its companion via Roche lobe overflow[1], forming an accretion disk around the compact object through conservation of angular momentum. The material eventually spirals into the deep gravitational well of the compact object, with potential of order 0.1 mc^2, and thus is heated to keV temperatures, causing the emission of X-rays. LMXBs are usually found in the bulge, disk and globular clusters of the Galaxy, whereas HMXBs (high-mass X-ray binaries with young massive stars as companions) are usually found near star-forming regions in the spiral arms of the Galactic plane. LMXBs are older than HMXBs. Her X-1 has a companion which is ~600 Myr old [5] and is considered to be an LMXB.

The accretion stream from HZ Her enters orbit around Her X-1 and forms an accretion disk (e.g. [24] [25]). Accretion onto Her X-1 from the inner edge of the disk proceeds through an accretion column, in which the hard X-rays (>1 keV) are produced [26] [27] [28] [29], and modulated by the rotation of theneutron star and the obscuration of the accretion disk. During the MH state the observer's view of the accretion column allows spectral studies of the accretion column as a function of neutron star rotation [30]. Spectral studies during the SH state show that there is an important component of X-ray scattering from the companion star [31]. A weaker flux of X-rays is present during low state and eclipses, which is scattered by extended matter in the system (e.g. [14] [15]).

However, there are other distinct X-ray flux modulations consisting of sharp and non-periodic absorption events, called lightcurve dips [32]. Spectral analyses

[1]The Roche-lobe is a teardrop-shaped volume around a star (in a binary) within which material is gravitationally bound to the star. Overflow occurs when the star expands beyond its Roche lobe, so material outside its Roche lobe orbits in the binary potential.

showing that dips were accompanied by absorption are presented by [33] [34]. These numerous dips occur throughout the orbital phase and the High states of the 35-day cycle, lasting from a few seconds to several hours in different intensities [35]. Dips were studied by [32], where their spectra showed X-ray absorption by cool material and Thomson scattering by ionized gas. According to [34] [36] dips can also be caused by partially ionized matter or by cool clumps of material immersed in hot ionized gas. [17] analyzed the pre-eclipse dips using RXTE/ASM data, confirming the marching phenomenon where the dips progress to earlier orbital phases as the 35-day phase increases. [24] modeled the stream-accretion disk impact and concluded that the dips properties can be explained by this model when the impact site of the accretion stream on the accretion disk obscures the X-ray source. The dips and orbital phase lightcurves were studied by [1] using RXTE/ASM, Swift Burst Alert Telescope (BAT) [37] and Monitor of All-sky X-ray Image (MAXI) [38] data. The absorption dips exhibit a drop in the SR simultaneous with a drop in the count rate. Ref. [39] reported a new phenomenon for dips during the MH state using the LAXPC instrument on board of the AstroSat Observatory [40]: several dips a showed constant SR as the count rate decreased instead of the usual behaviour for absorption dips. These dips could be caused by highly ionized matter blocking the X-rays (and so the spectrum doesn't change as the count rate decreases), or by partial coverage of very dense matter.

Ionized gas in Her X-1 was demonstrated by [2]. [41] presented a model for the large-scale electron scattering corona by analyzing RXTE/PCA eclipse lightcurves in the MH state. The corona was approximated by a spherically symmetric electron density distribution, since a more detailed corona would not be justified due to the large errors in the mid-eclipse lightcurve. Their model allows for three possible scenarios: the expected temperature from heating by Compton scattering is similar to that required to keep the corona in hydrostatic equilibrium; the entire corona is a fast outflow; or the corona could be hybrid, with an inner hydrostatic region and an outer-low region with low outflow velocity. In addition, they detected a bump in the eclipse lightcurve at orbital phase 0.945 (eclipse ingress) which could be caused by the impact of the accretion stream with the disk [24].

The main objective of the current work is to create high sensitivity 35-day RXTE/PCA lightcurves for Her X-1 which have the best 35-day phase as possible. For this we use Swift/BAT and RXTE/ASM data which overlap in time with the RXTE/PCA data. Correctly phased 35-day lightcurves with high sensitivity and good time resolution are needed to study and model the accretion disk in Her X-1. Related objectives are to measure systematic changes in orbital lightcurves and eclipse shapes with 35-day phase. A secondary objective is to confirm the no-absorption dips detected in AstroSat/LAXPC data by [39], using the RXTE/PCA data which has similar sensitivity. Section 2 describes the data and analysis; and Section 3 presents the lightcurves. In Section 4 we discuss the new results and conclude in Section 5.

2. Data and Analysis

2.1. Rossi X-Ray Timing Explorer (RXTE) Observations

The Rossi X-ray Timing Explorer (RXTE) collected 16 years (from its launch in December 1995 to January 2012) of data on the X-ray variations of high-energy sources (e.g., black holes, neutron stars, or pulsars, among others). The spacecraft carried the Proportional Counter Array (PCA) [42] covering the energy range 2 - 60 keV, with geometric area of 6500 cm^2 and time resolution of 1 microsec. It also carried the High Energy X-ray Timing Experiment (HEXTE) [43] covering an energy range of 15 - 250 keV, with geometric area of 2×800 cm^2 and the All-Sky Monitor (ASM) [44] covering and an energy range 2 - 10 keV and a sensitivity of 30 mCrab.

Here we analyze the RXTE/PCA data. The data were downloaded from the NASA's High Energy Astrophysics Science Archive Research Center (HEASARC) web site (https://heasarc.gsfc.nasa.gov), which is a data archive for high energy astrophysics missions. The list of observations (start and end times in MJD) is given in Table 1.

Table 1. RXTE/PCA observations of Her X-1.

MJD start	MJD end	Exposure time (ks)
50290.03	50291.45	47.84
50340.99	50380.92	56.69
50690.31	50728.41	151.87
50773.87	50774.90	22.72
51000.27	51007.85	71.28
51294.41	51294.64	10.06
51370.83	51375.44	90.26
51443.86	51443.96	6.19
51621.34	51623.15	19.58
51833.04	51833.40	18.78
51869.15	51933.81	108.34
52032.98	52099.26	232.26
52243.26	52269.49	280.42
52454.20	52493.14	32.05
52595.06	52634.15	288.00
52734.60	52734.96	18.40
52908.17	52908.47	15.82
52950.03	52950.39	18.02
53037.48	53058.96	83.66
53199.02	53202.11	10.00
53235.57	53237.76	10.64

Continued

53300.77	53301.13	18.40
53367.15	53367.18	3.17
53527.98	53539.00	33.20
53573.01	53584.32	36.34
54866.56	54866.99	22.69
55564.75	55570.86	81.28

2.2. Analysis

The downloaded data contains 23 folders, one for each observing proposal. The standard products for bands b (2 - 4 keV), c (4 - 9 keV), and d (9 - 20 keV) were used in the current analysis. Using the standard lightcurve files, we calculate time (in Modified Julian Day), orbital phase, 35-day phase, softness ratio and its error. The time units in seconds have been converted to Modified Julian Date in Terrestrial Time using the conversion:

$$MJDB = \frac{TDB}{24*3600} + MJDB_{ref}\left(TT\right) \tag{1}$$

where TDB is the barytime, and $MJDB_{ref}\left(TT\right)$ is the reference time of the instrument: $MJDB_{ref}\left(TT\right) = MJDB_{ref,int} + MJDB_{ref,frac} = 49353.000696574076$ d.

For the calculation of the orbital ephemeris, we use:

$$P_{orb}\left(t\right) = P_{orb}\left(0\right) + \left(MJD - T_{\pi/2}\left(0\right)\right) * \dot{P}_{orb}\left(0\right) \tag{2}$$

where we use the constants from Table 3 of [4]: $T_{\pi/2}\left(0\right) = 46359.871940$, $P_{orb}\left(0\right) = 1.70016759$, and $\dot{P}_{orb}\left(0\right) = -4.85\times10^{-11}$. The average orbital period over time $T_{\pi/2}\left(0\right)$ to time t is:

$$P_{av}\left(t\right) = \frac{P_{orb}\left(0\right) + P_{orb}\left(t\right)}{2} \tag{3}$$

because the orbital period is increasing linearly with time. The time T from the reference time is $T = t - T_{\pi/2}\left(0\right)$. The orbital phase, ϕ_{orb}, with phase reference 0 defined as mid-eclipse of the neutron star by the companion star, is given by the fractional part of $\frac{T}{P_{av}\left(t\right)}$. and the number of orbital cycles, n, is given by the integer part of $\frac{T}{P_{av}\left(t\right)}$. The softness ratio, SR, here for band b over band d, is given by:

$$SR = \frac{b}{d} \tag{4}$$

with b and d the count rates in bands b and d, respectively.

2.3. Anomalous Low States

The data were first filtered to remove the Anomalous Low States (ALS1 and ALS2, also referred to as the 2000 and 2004 ALS's). To remove ALS1 and

ALS2, we first used the intervals measured by [18] (their Table 1: MJD51256 to MJD51757 and MJD52946 to MJD53159). Ref. [45] gives similar intervals for the 2000 ALS, as MJD51224 to MJD51826, and the 2004 ALS, as MJD52945 to MJD53157. They also give an ALS from MJD57302 to MJD57372, however for that period the 35-day cycle is seen in the Swift/BAT data ([16]). We then we reexamined the ASM, BAT and PCA lightcurves, which led us to refine the ALS1 and ALS2 periods: from MJD 51230 (Feb. 21, 1999) to 51755 (July 30, 2000) for ALS1, and from MJD 52980 (Dec. 7, 2003) to 53100 (Apr. 5, 2004) for ALS2.

2.4. 35-Day Phase Determination

35-day phase, ϕ_{35}, was calculated as:

$$\phi_{35} = \frac{t - t_n^{35}}{P_n^{35}} = \frac{t - t_n^{35}}{t_{n+1}^{35} - t_n^{35}} \tag{5}$$

where t is time of the data, t_n^{35} is the reference time and P_n^{35} is the length of 35-day cycle number n.

Her X-1 was observed during a long-term monitoring campaign by RXTE/ASM and Swift/BAT. The values of t_n^{35} and P_n^{35} [16] were determined by a cross-correlation analysis of the data with a 35-day template lightcurve. Tables 1 and 2 of [16] are used here because ASM and BAT values of t_n^{35} and P_n^{35} cover the same time period as the RXTE/PCA data. Unlike the RXTE/ASM and the Swift/BAT data, the cross-correlation method does not work well for the RXTE/PCA data: the PCA data are mostly spaced irregularly with large gaps (Fig. 1 of [11]) with poor coverage of 35-day cycles. The PCA data consists of $\simeq 1.4 \times 10^6$ s integration time over a period of $\simeq 4.6 \times 10^8$ s. The cross-correlation does not give clear peaks except for very few of the PCA observations which have coverage of the peak of MH state.

The tables of t_n^{35} and P_n^{35} from [16] consist of two parts: an interval of MJD 50146.553 to 53403.780 taken from the ASM table, and an interval of MJD 53437.822 to 58691.994 taken from the BAT table. The first part contains 94 cycles of ASM data and the latter contains 152 cycles of BAT data giving a total of 246 cycles[2]. The uncertainties of 35-day phase determination from ASM and BAT are discussed in Section 4 of [16]. The mean accuracy of the cycle lengths from the ASM and BAT analysis is ±0.75 d, with a few errors exceeding 3 d (see Fig. 8 of [16]).

The characteristic shape of the 35-day average lightcurve is well-determined from ASM, BAT and MAXI monitoring observations ([16] for ASM and BAT, [46] for BAT and MAXI)[3]. The plots of RXTE/PCA count rate vs. ASM/BAT-determined 35-day phase show some incorrectly phased data, out of place compared to the characteristic shape of the 35-day lightcurve. The incorrect phasing

[2]In the original ASM/BAT table, a total of 248 cycles were listed because of the repetition of BAT cycles 3 and 4. The original cycle numbering of the ASM table was kept, but the numbering of the BAT table was changed to be consecutive with the ASM numbering (cycle 0 was renumbered 97, etc., the same as in Table 4 of [16]).

[3]This is subject to phase errors of ~±1.5 d, to the lower sensitivity of monitoring observations, and to variability in the 35-day cycle.

is caused by known errors in ASM/BAT-determined 35-day phase. The errors in phase were found by examing the PCA count rates and SR vs. ASM/BAT 35-day phase. E.g. data with high count rate during LS indicated that it belonged to either MH or SH states, and a 35-day phase adjustment was needed to move it out of LS. The group of points for cycles 97 and 98 between ASM/BAT phase $0.63 \le \phi_{35} \le 0.64$ with low count rate (5.88 ≤ Band b ≤ 9.15) indicating a 35-day cycle length adjustment for those cycles. We note that the phase adjustments were applied only to the 35-day cycle times, t_n^{35} and P_n^{35}, which changes only the calculated 35-day phase of the data points. All of the adjustments are listed in Table 2, ranging from 1.0 to 3.4 d. The mean adjustment of 1.7 d is consistent with the estimated ASM/BAT 35-d phase measurement errors. After these adjustments the 35-day lightcurve showed no clearly-outlying data.

The resulting 23 cycles which have RXTE/PCA observations are plotted in separate colors in Figure 2. The cycles plotted together in each panel were selected to have the least amount of overlap in 35-day phase. The longest PCA observation is that for cycle 62 (~10 d). Eight cycles have short ($\lesssim$1 d) PCA observations: cycles 67, 75, 80, 91, 93, 100, 136 and 156.

3. Results

3.1. 35-Day Phase Lightcurves

Figure 3 (top panel) shows the resulting 35-day lightcurve including all of the PCA data, with the phase adjustments of Table 2. The lower panel shows SR vs. 35-day phase and illustrates the large number of dips (and a smaller number of eclipses) where absorption by cold matter occurs, causing SR to drop below 0.3 simultaneously with a drop in count rate[4]. For out-of-dip times in MH, SR ranges from 0.3 to 0.55 and in SH, SR ranges from 0.3 to 0.7.

We divide the 35-day cycle into the eight substates as listed in Table 3. Early published work on Her X-1 recognized MH, SH and LS and later work sub-divided MH into MH turn-on, MH and MH decline; SH into SH turn-on, SH and SH decline and LS into LS1 and LS2 (e.g. [14]). We initially used the 35-day phases for the eight substates of the 35-day cycle summarized by [46] (their Table 2).

Table 2. Modified 35-day cycle peak times.

Cycle	New cycle no.	New peak time	Days added
ASM 59	59	52107.6	1
ASM 81	81	52879.2	1.2
ASM 82	82	52916.5	1.2
BAT 1	97	53477.0	2
BAT 2	98	53509.6	3.4
BAT 3	99	53544.8	1.4
BAT 4	100	53581.9	1.9

[4]SR values below 0.3 indicate absorption by cold matter [35].

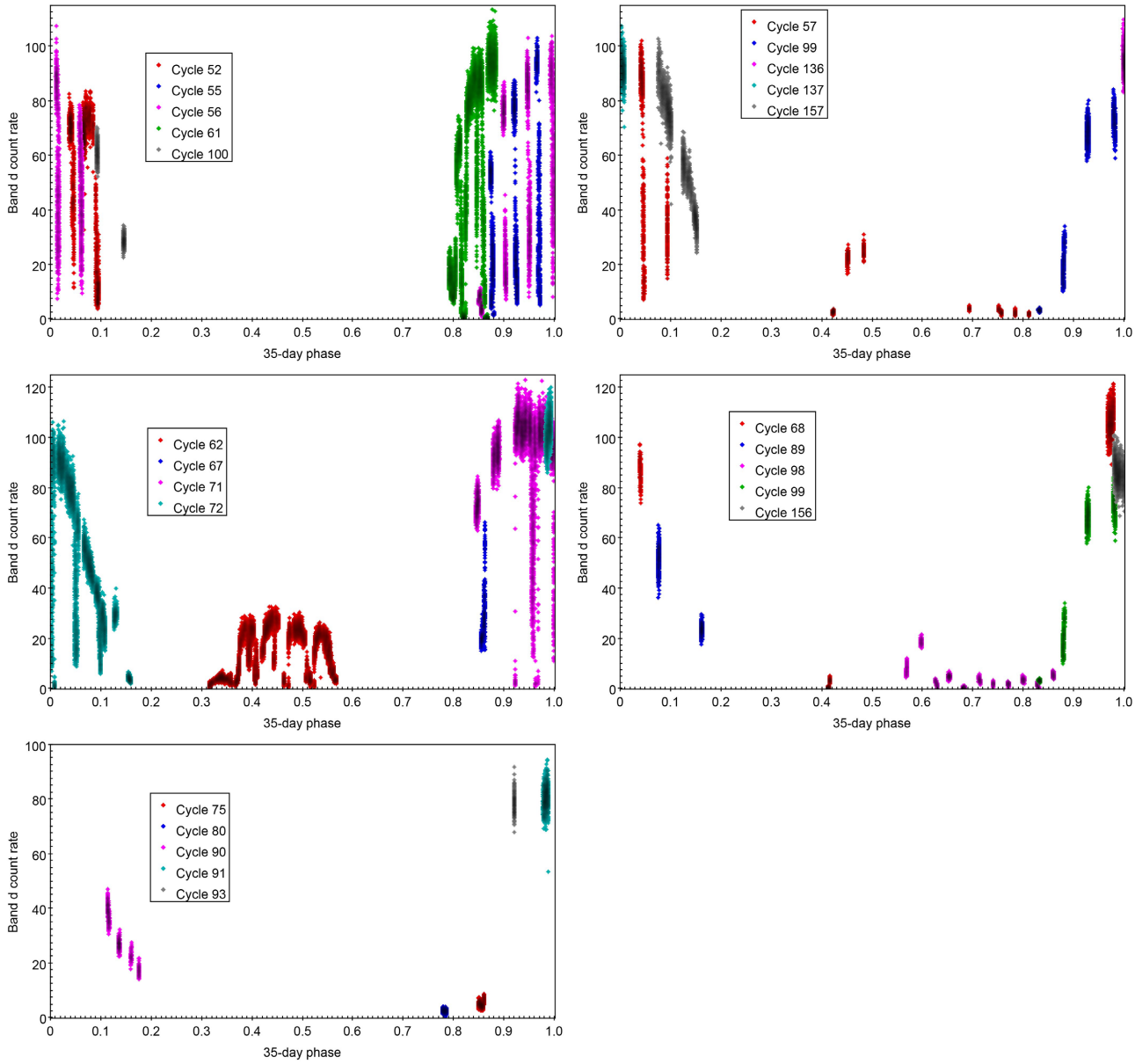

Figure 2. Individual 35-day cycle RXTE/PCA lightcurves of Her X-1 for Band d (9 - 20 keV) for the 23 observed cycles, including the phase adjustments of **Table 2**.

Table 3. Definition of substate intervals in 35-day phase for PCA data.

State	Start phase	End phase	Duration
MH Turn-on	0.786	0.815	0.029
MH	0.815	0.997	0.182
MH decline	0.997	0.180	0.183
LS1	0.180	0.368	0.188
SH Turn-on	0.368	0.379	0.011
SH	0.379	0.454	0.075
SH decline	0.454	0.624	0.170
LS2	0.624	0.786	0.162

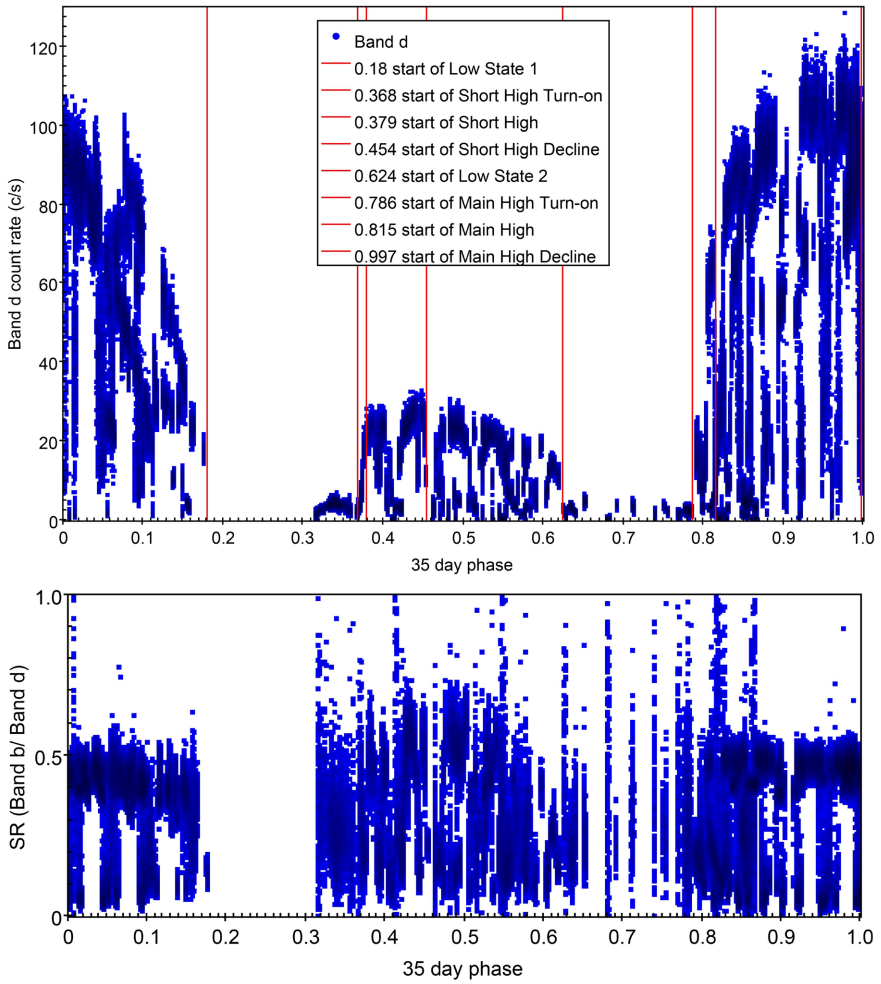

Figure 3. 35-day cycle RXTE/PCA lightcurve of Her X-1 for Band d (9 - 20 keV, top) and softness ratio SR (Band b/Band d, bottom). The dashed lines delimit the intervals for each substate. These include all observations of Her X-1 by RXTE/PCA. The points with SR $\lesssim$ 0.3 are those that show cold matter absorption.

However, with the higher sensitivity of the RXTE/PCA data compared to the ASM or BAT data, we were able to better determine the 35-day phase boundaries of the states. The boundaries were determined as follows. LS1 and LS2 were defined by the periods of persistent low Band d count rate. The MH decline and SH decline were defined by the start and end of the slow declines of count rate during MH and SH, respectively. The MH turn-on and SH turn-on were defined by the beginning and end of the rapid phases of increase of count rate at the start of MH and SH. The remaining slow rise and constant count rate parts of MH and SH defined the MH and SH intervals.

The adjusted 35-day phase boundaries of the substates are shown as vertical lines in **Figure 3** (top panel). The 35-day lightcurve for the PCA data show a fast turn-on and a slow decline for MH and for SH states. All eight substates are better defined by the PCA 35-day lightcurve here compared to the BAT or ASM 35-day lightcurves [16] because of the higher sensitivity of the PCA data, the

updated 35-day cycle timing here, and the ability to separate dip data from non-dip data.

A binned 35-day lightcurve (data averaged into 100 equally spaced phase bins) is shown in Figure 4. To create this we removed eclipse data (including ingress and egress) between orbital phases 0.00 - 0.09 and 0.91 - 1.00, which removed ≃7400 times from the original ≃97,500. Then we removed dip data so that we do not average dip and non-dip data by removing data with SR < 0.3, which removed another ≃29,700 data points. This removed most of the dips but not the lowest count rate part of the dips where the SR increases again (see Figure 9 below). To remove these dip points we removed data points with Band d count rate < 12 c/s for all states except LS1 and LS2. LS1 and LS2 had 964 and 1028 data points, respectively. The remaining data are plotted against the 35-day phase in Figure 4 (blue points). The red curve is the result of averaging the data into 100 phase bins. The variability of the lightcurves for the 16 different MH states observed by RXTE/PCA has been shown in Figures 2 and 3 of [47]. Comparison of the PCA data plotted against MJD shows that the binned lightcurve is significantly distorted by combining data from different 35-day cycles of different peak brightness and by the uneven sampling.

3.2. Orbital Phase Lightcurves

Orbital lightcurves generated for Band d and SR (Band b/Band d) are shown in Figure 5, for MH and MH turn-on (left panel) and for MH decline (right panel). Band d and SR lightcurves are shown in Figure 6 for SH, SH decline and SH turn-on (left panel), and for LS1 and LS2 (right panel).

The decline of MH and of SH is not clearly shown by panel (c) in Figure 5 and panel (c) in Figure 6. This is because the declines for MH and SH each last several orbits, and because there are different 35-day cycles with different strengths

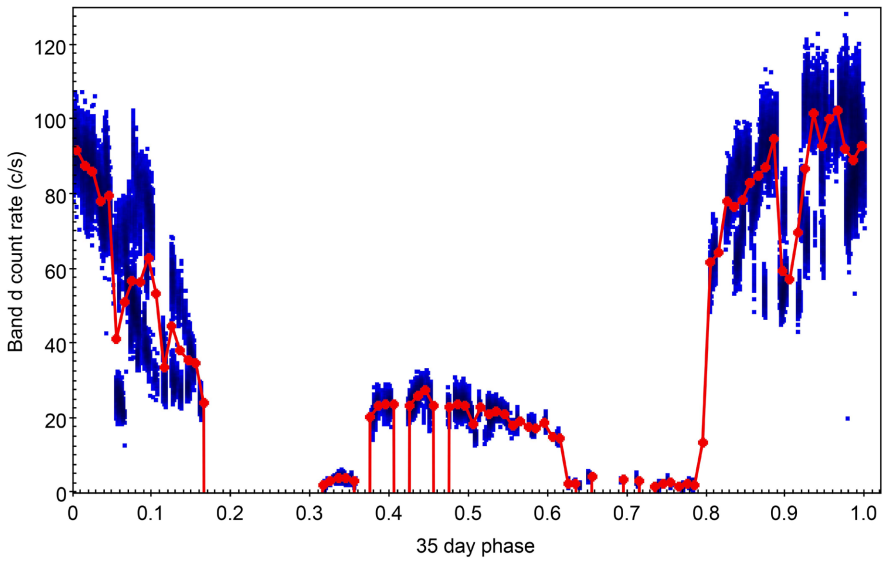

Figure 4. The binned 35-day cycle RXTE/PCA lightcurve of Her X-1 (red line). Eclipses and dips were removed prior to binning which yielded the 35-day lightcurve (blue points).

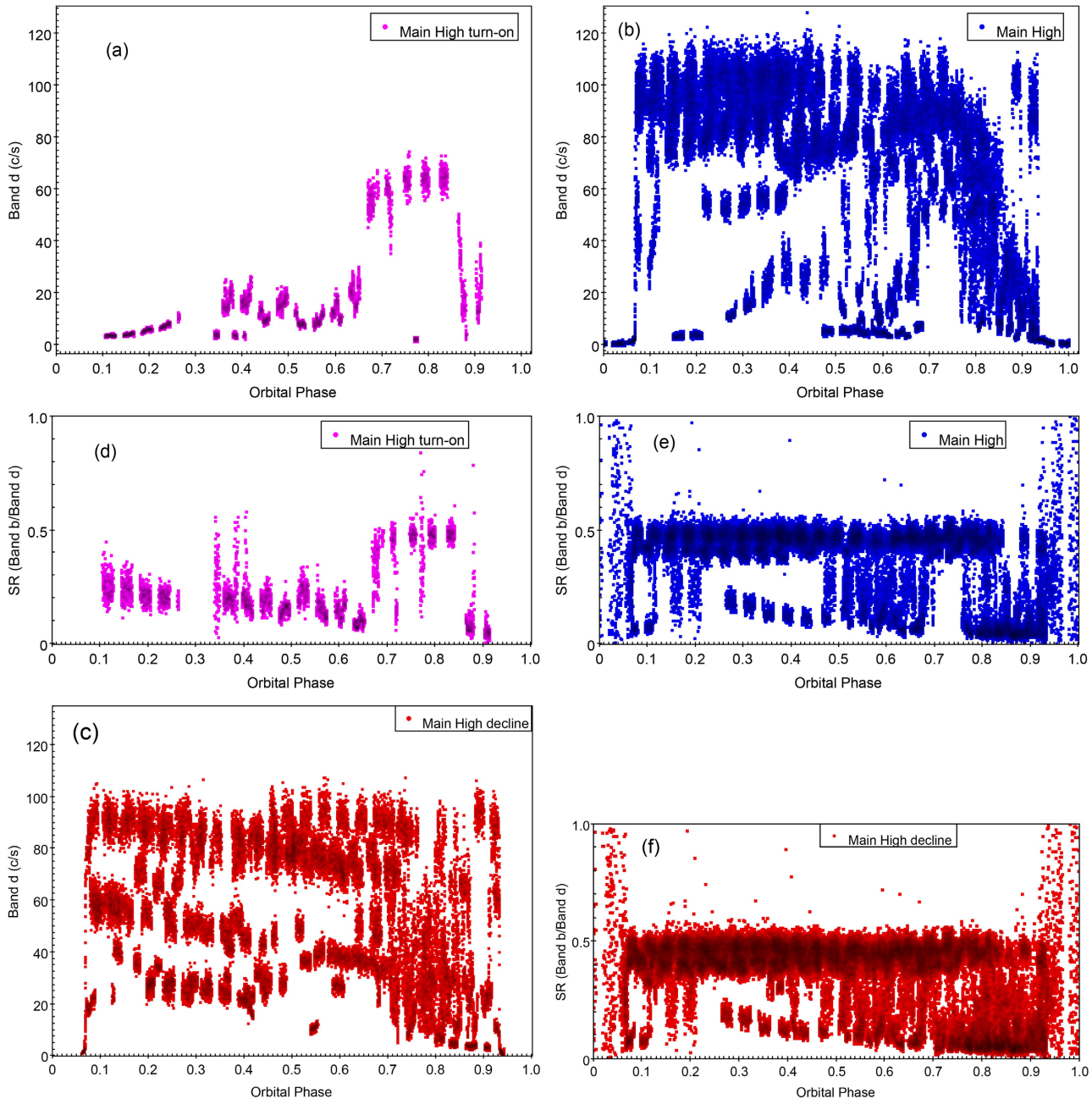

Figure 5. Orbital phase Band d lightcurves for (a) MH turn-on; (b) MH; and (c) MH decline. SR vs. orbital phase for: (d) MH turn-on; (e) MH; and (f) MH decline.

(maximum Band d count rate) plotted together. To show the decline, the 20 orbits that make up the SH decline are plotted separately in Figure 7. The decline can now been seen in the successive orbits for the different 35-day cycles (noted in the Figure caption). This also shows the variability between of SH decline between different 35-day cycles. Similar properties (the variability and the decline within a given 35-day cycle) apply to MH decline, however the number of orbits observed for MH decline is significantly larger (~50) making it more difficult to identify trends.

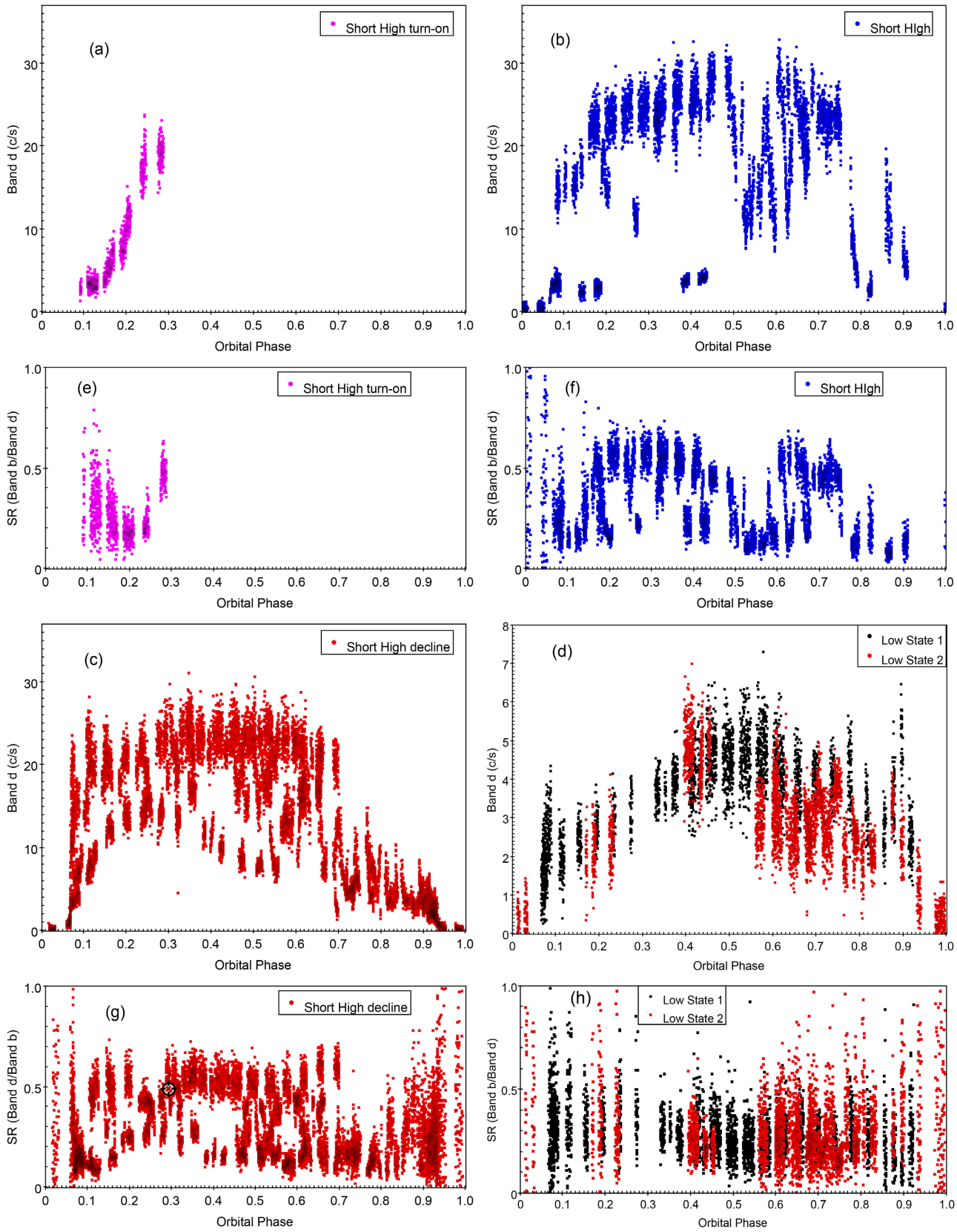

Figure 6. Orbital phase Band d lightcurves for (a) SH turn-on, (b) SH, (c) SH decline and (d) LS 1 and 2. SR vs. orbital phase for: (e) SH turn-on, (f) SH and (g) SH decline and (h) LS 1 and 2.

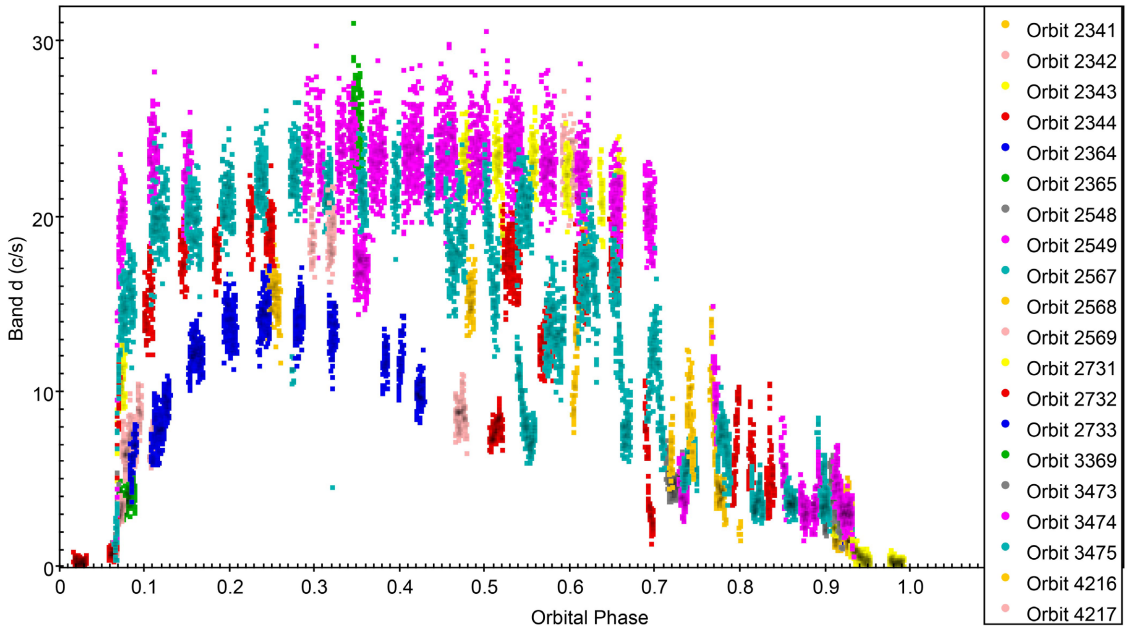

Figure 7. Orbital phase Band d lightcurves for SH decline, showing the 20 individual binary orbits of data which make up the light curve. The decline with 35 day phase is seen as successive orbits with lower amplitude (Orbits 2341 to 2344 for one 35-day cycle; 2364 and 2365 for the next; 2548 and 2549 for another; 2567 to 2569 for another; 2371 to 2373 for another; 3473 to 3475 for another; and 4216 and 4217 for the last observed 35-day cycle).

3.3. Eclipse Lightcurves

Eclipses during MH are well defined and occur over orbital phases 0 to 0.07 for egress and 0.93 to 1.0 for ingress (e.g. Fig. 1 of [5]). To clearly see the eclipse lightcurves, some data on either side of eclipse is included here, i.e. the orbital phases plotted are extended to 0 to 0.1 and 0.9 to 1.0. 1 has been added to the 0.0 to 0.1 orbital phase data to make the phase continuous across the eclipse (0.9 to 1.1). Due to the large dynamic range of count rates, the resulting lightcurves are plotted on logarithmic scale. **Figure 8** shows the eclipse lightcurves in Band d for MH, MH decline and MH turn-on (top left); for SH, SH decline and SH turn-on (top right) and for LS1 and LS2 (lower panel). The scatter of the points is explained by countrate errors. For the weak count rates the relative errors are the largest, e.g. 0.5 c/s has a typical error of ≈0.35 - 0.45 c/s.

4. Discussion

4.1. 35-Day Phase Lightcurves

The unbinned 35-day lightcurves are shown in the upper panel of **Figure 3**. The lower panel shows the SR, which indicates absorption by a value $\lesssim 0.3$ and no absorption by a value $\gtrsim 0.3$. The relation between SR and absorption by dips was demonstrated by [34] [35] and absorption by companion eclipses by [48]. The time resolution of the ASM and BAT lightcurves [16] was low enough that most dips are not resolved so that dip and non-dip data are mixed. However, the 16 s time resolution of the PCA standard products is sufficient to resolve and separate dip data from non-dip data [35].

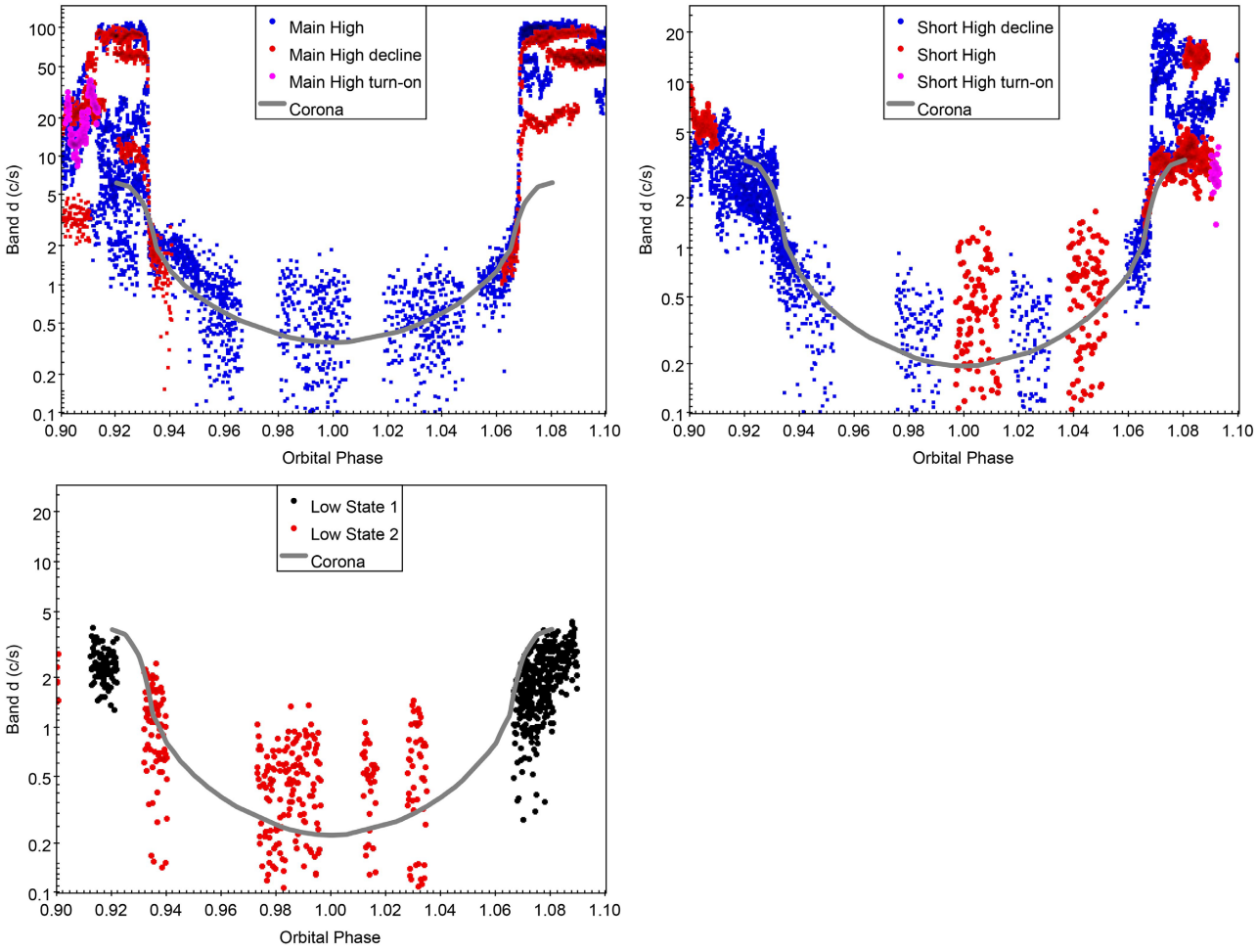

Figure 8. 9 - 20 keV (Band d) eclipse lightcurves for MH, MH decline and MH turn-on (top left panel); for SH decline, SH and SH turn-on (top right panel) and for LS 1 and LS 2 (bottom panel). The grey line is the coronal scattering model from [41].

The PCA 35-day lightcurve shows numerous dips, consistent with the finding by [11] that for a significant fraction of the time Her X-1 shows absorption. After removing the absorbed data with SR < 0.3, the 35-day lightcurve retains a factor ~2 variation at any given 35-day phase. This was previously known from the long record of 35-day cycle strengths from ASM and BAT (e.g. Fig.1 of [18] for ASM or Fig.2 of [16] for BAT). The PCA 35-day lightcurve presented here will be a valuable input for models of the 35-day cycle which are used to constrain the shape of the accretion disk, similar to the work of [8] [15].

4.2. Orbital Lightcurves

A recent study of orbital X-ray lightcurves of Her X-1 was done by [1] using RXTE/ASM, MAXI and Swift/BAT data. That considered the six 35-day substates of MH turn-on, MH, MH decline, LS 1, SH combined (SH turn-on, SH and SH decline) and LS 2, then subdivided MH into four pieces (MH-a, MH-b, MH-c and MH-d) for study of the main dip progression with 35-day phase. With the low sensitivity of ASM, MAXI and BAT data and the long-term obser-

vations, the orbital lightcurves were created using binned data. The PCA data analysed here has much higher sensitivity (smaller errors by a factor of ~10). This allows creation of PCA lightcurves for the eight 35-day substates using unbinned data, which reveals the dips and the variability of Her X-1 at each orbital phase.

The MAXI, BAT and ASM lightcurves from [1] (their Fig.1 and Fig. A1) show significant differences between the different 35-day substates, which can be compared to what is seen in the PCA lightcurves (**Figure 5** and **Figure 6**). In particular, for MH the lightcurve is nearly flat-topped except near eclipse egress and for dips after orbital phase ~0.75. The better time resolution and sensitivity of the PCA data show that MH has a rapid rise at eclipse egress not seen in the MAXI, BAT and ASM lightcurves. The bump at orbital phase 0.9 in the MAXI/BAT/ASM lightcurves is seen by the PCA data to be caused by a mixture of unabsorbed data with absorbed data, which are not time-resolved in the MAXI/BAT/ASM data. For MH turn-on, the BAT/MAXI/ASM lightcurves show two maxima at orbital phases 0.3 and 0.8; however, the PCA data shows only a single maximum at orbital phase 0.8. This is probably due to the incomplete coverage of different 35-day cycles by the PCA, so it missed catching MH turn-ons near orbital phase 0.3. The MH decline for the BAT/MAXI/ASM lightcurves has a dip at orbital phase 0.4 which is seen in the PCA MH decline lightcurve (**Figure 5**).

For SH, the PCA lightcurve has a smooth maximum near orbital phase 0.4 similar to that seen in the BAT/MAXI/ASM lightcurves. For the BAT/MAXI/ASM SH lightcurves, late orbital phases ($\gtrsim$0.5) are quite weak. The PCA SH lightcurves show that this is caused by the much higher incidence of dips after orbital phase 0.5 ((c) of **Figure 6**). The LS 1 and 2 lightcurves show clear modulation in the PCA data not seen in the BAT/MAXI/ASM SH data, because of the lower sensitivity and larger background uncertainties for the latter.

4.3. Eclipse Lightcurves

A new result here is that eclipse lightcurves (**Figure 8**) have now been produced for states other than MH, including MH decline, SH, SH decline and the Low States 1 and 2. The evidence for a bowl-shaped eclipse, previously known for MH only, is now demonstrated for these other states. The evidence is clear for the six MH and SH substates. Because of the large number of data points during eclipse, the statistical evidence for the bowl-shaped emission during eclipse is very strong (e.g. for MH see [41]). The evidence is less secure for the Low States, because of the incomplete observations. Future observations of eclipses with other instruments with better time coverage of LS, such as those on the AstroSat satellite, could confirm the bowl-shaped eclipses for the LS.

Ref. [41] analyzed binned data for MH eclipses using a corona model. The bowl-shaped eclipse is evidence for an extended electron scattering corona in the binary system: it has to be larger than the companion star HZ Her, in order to yield residual X-ray flux at mid-eclipse. The unbinned eclipse data presented

here in Fig. 7 shows that the lower pre-ingress flux than post-egress flux for MH is caused by more numerous dips in the pre-ingress period than in the post-egress period, rather than a different flux emitted by the neutron star.

The corona model from [41] was fitted to the new eclipse lightcurves here for substates with enough data: MH, MH decline, SH, SH decline, and the combined data from Low States 1 and 2. The phase interval from post-stellar ingress (0.932) to pre-stellar-egress (1.068) was fit using χ^2 minimization with normalization C as the single fit parameter. The corona model lightcurves (without companion ingress and egress models) are shown in **Figure 8**. **Table 4** shows the results of the fits, with C, χ^2 and χ^2/dof values, where dof means degrees of freedom.

Ref. [41] (their Figure 4) shows an excess at orbital phase 0.94 above the coronal model best fit for MH eclipse. We verify the excess here for MH: the fit of the coronal model to data not including the excess region (orbital phase 0.935 to 0.96) is a significant improvement over the fit to data including the excess region (see comparison of "MH" and "MH no excess" fits in **Table 4**, decrease in χ^2 of 940 for a decrease of 531 in dof). For the other states, the data are too sparse to determine whether there is an excess at similar or different orbital phases during the eclipse. The proposed explanation of the excess is scattered X-rays from the accretion stream. The changing geometry of the accretion stream and its impact site on the accretion disk surface, described by the model of [24], implies that the excess should change its orbital phase with 35-day cycle phase. More complete observation of eclipses for different 35-day phases are needed in order to test this.

Table 4 shows that the normalization of the corona, C, is similar for MH (no excess) and MH decline (by $<3\sigma$) but significantly lower for SH and SH decline (SH lower than MH decline by $\sim 4\sigma$ and SH decline lower than MH decline by $\sim 10\sigma$). The normalizations for SH, SH decline and LS differ by $<3\sigma$. Some change in the normalization of intensity from the corona is expected because the changing orientation of the accretion disk implies changing visibility of the inner regions of the corona. More complete observations of the eclipses would allow

Table 4. Fits of coronal model to eclipses[a].

35-day State	C[b] (1σ error)	χ^2	dof	χ^2/dof
MH	1.273 (0.014)	1630	1531	1.065
MH no excess[c]	1.048 (0.019)	690	1000	0.690
MHdec	0.953 (0.028)	66	94	0.702
SH	0.71 (0.07)	174	278	0.626
SHdec	0.599 (0.013)	437	634	0.689
LS1 + 2	0.75 (0.05)	204	3770	0.550

(a): MH turn-on and SH turn-on did not have enough data to fit; LS 1 and LS 2 data were combined into LS1 + 2; the orbital phases of eclipse that were fit are 0.0935 to 1.065. (b): 1σ errors are given in brackets. (c): for this fit the region with the excess between phases 0.935 and 0.960 was omitted.

testing the shape of the corona by applying a model for the partial eclipse of the corona by the rotating accretion disk shape (**Figure 1**).

4.4. Absorption Dips and No-Absorption Dips

As noted above, absorption dips are identified by a decrease in SR that coincides with a decrease in count rate, whereas no-absorption dips show no change in SR as the count rate decreases. To identify both types of dips, SR vs. count rate was examined for each state. Eclipses (orbital phases 0.0 to 0.07 and 0.93 to 1.0) were filtered out of the data prior to the search.

Figure 9 (left panel) shows the resulting SR vs. band d count rate for the MH turn-on, MH and MH decline (with the MH on points superimposed on the MH decline points to better see the three sets; the MH decline points cover the entire region below the MH points) Absorption dips can be seen by the sharp decrease in SR for the points below the main cluster of unabsorbed data which lies between SR of 0.4 and 0.5. Although there are small decreases in count rate without decreases in SR (without absorption) within the main cluster of points, there are no deep drops in count rate without a drop in SR. *I.e.*, we don't find any no-absorption dips in the MH states.

The right panel of **Figure 9** shows SR vs. band d count rate for the LS (combined), SH turn-on, SH decline and SH (with the LS points plotted on top, then SH turn-on, then SH decline, and SH below). Absorption dips in the three SH states are identified by the drop in SR below 0.3 associated with a decrease in band d count rate. For the SH states the fraction of data showing absorption is ~70%, in contrast to the MH states with a proportion of data with absorption of ~30%., consistent with [11]. The errors in SR for LS points (and all other points with count rate $\lesssim 6$) are large enough that absorption (or its absence) cannot be detected.

The previous report of no-absorption dips by [39] used 5 - 9 and 9 - 20 keV bands from Large Area X-ray Proportional Counter (LAXPC) on Astrosat. For a closer comparison to this analysis we analysed SR vs count rate with SR given by PCA Bands c (4 - 9 keV) and d (9 - 20 keV). Using SR = Band c/Band d results in absorption dips following a nearly linear decrease of SR with count rate, in agreement with [39] (their Fig.7) instead of the curved trajectory of points for SR = band B/Band d as seen in **Figure 9** here. However, we found no no-absorption dips in the PCA data.

In summary, we did not find any no-absorption dips in our thorough search. We checked two different definitions of SR, and searched all three MH states and all three SH states in the entire RXTE/PCA archive of observations of Her X-1. The AstroSat collaboration has updated the LAXPC data processing software including a new background model (see http://astrosat-ssc.iucaa.in/laxpcData). Thus it is possible that the detection of no-absorption dips by [39] was caused by errors in background subtraction using the older data analysis package.

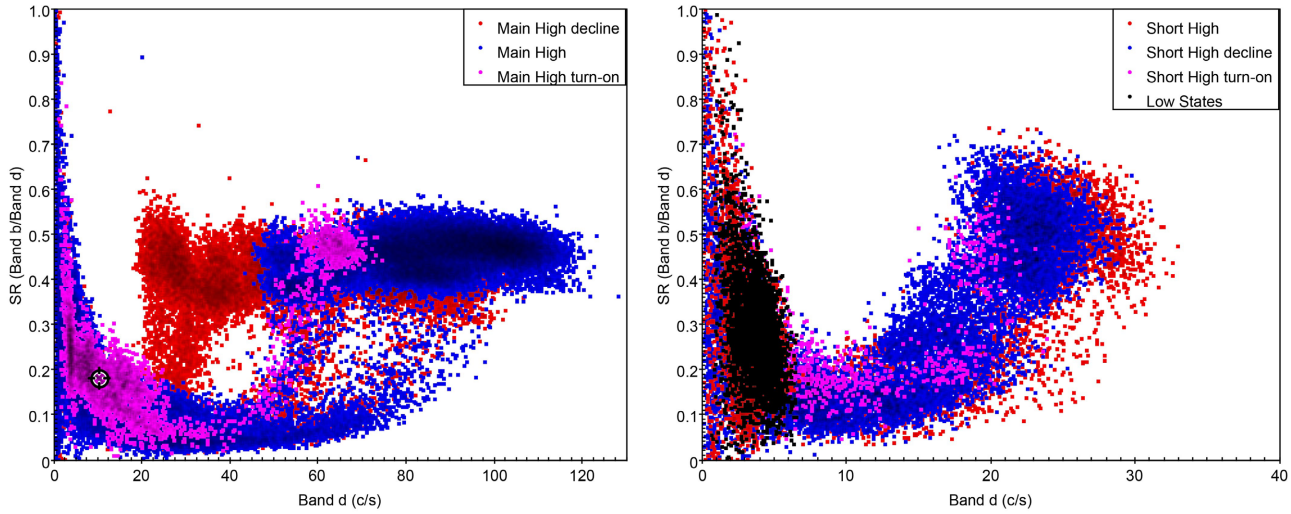

Figure 9. SR vs. count rate plots for the different 35-day states. Left panel: for MH turn-on, MH and MH decline. Right panel: for SH turn-on, SH, SH decline and Low States (1 and 2 combined). Dips in the MH states correspond to the points below the main cluster of points between count rates of 20 to 120 c/s. Dips in the SH states correspond to the points below the main cluster of points between count rates of 17 to 30 c/s.

5. Conclusions

We report an analysis of the entire archive of Standard 2 data on Her X-1 collected by the RXTE/PCA instrument to generate lightcurves for 35-day phase, orbital phase and eclipses. The start times and lengths of the 35-day cycles observed by PCA are updated from initial values derived from RXTE/ASM and Swift/BAT observations [16] to be consistent with the PCA data. Using the higher sensitivity 35-day lightcurve from PCA, the boundaries of the eight substates of the 35-day cycle (*i.e.* MH turn-on, MH, MH decline, LS 1, SH turn-on, SH, SH decline and LS 2) are refined, and the boundaries of the ALS are adjusted to be more accurate. For MH a rapid turn-on is seen followed by a slow rise to peak and a slow decline. SH follows a similar pattern but peaks at ~25% of the MH peak. Absorption dips are present throughout the MH and SH states, and are more prevalent during SH. The orbital lightcurves for the different 35-day states show a progression of changes with 35-day phase similar to those demonstrated in ASM and BAT data [1] [17], but with clear identification of the significance of the dips on the lightcurves, using SR. The data coverage of the LS states is incomplete and will require further observations with newer X-ray instruments.

Eclipse lightcurves of Her X-1 are generated for the different 35-day states, and show that the bowl-shape during eclipse is present for all states. The PCA data show that the extended scattering corona, found during MH [41], is present for the entire 35-day cycle. The scattered intensity from the corona changes significantly but only over a moderate range (C in rows 2 to 6 of **Table 4** has a minimum of 0.6 and a maximum of 1.05) with 35-day phase, which is consistent with a corona larger than the accretion disk, which is partially blocked by the disk as the disk rotates with 35-day phase.

A search for dips using the 2 - 5, 5 - 9 and 9 - 20 keV PCA data (bands b, c and d) is carried out. The standard absorption dips are found. However, we do not find any no-absorption dips similar to those reported by [39] in any of the MH or SH states in the entire PCA archive of Her X-1 data. Because the sensitivity of RXTE/PCA is similar to that of AstroSat/LAXPC, any no-absorption dips observed should have been detected. In future work, the LAXPC data can be reanalysed with the updated LAXPC analysis software and updated background model. If the no-absorption dips are verified in LAXPC data, then these must be a rare phenomenon not detected by the PCA instrument.

Acknowledgements

This work supported by the Natural Sciences and Engineering Research Council and by MITACS through their Globalink student exchange program.

Conflicts of Interest

The authors declare no conflicts of interest regarding the publication of this paper.

References

[1] Wang, Y. and Leahy, D. (2022) The Evolution of the Orbital Lightcurve of Hercules X-1 with 35 Day Phase. *The Astrophysical Journal*, **927**, Article No. 143. https://doi.org/10.3847/1538-4357/ac496f

[2] Ji, L., Schulz, N., Nowak, M., Marshall, H. and Kallman, T. (2009) The Photoionized Accretion Disk in Her X-1. *The Astrophysical Journal*, **700**, Article No. 977. https://doi.org/10.1088/0004-637X/700/2/977

[3] Klochkov, D., Staubert, R., Postnov, K., Shakura, N. and Santangelo, A. (2009) Continuous Monitoring of Pulse Period Variations in Hercules X-1 Using Swift/BAT. *Astronomy and Astrophysics*, **506**, 1261-1267. https://doi.org/10.1051/0004-6361/200912791

[4] Staubert, R., Klochkov, D. and Wilms, J. (2009) Updating the Orbital Ephemeris of Hercules X-1; Rate of Decay and Eccentricity of the Orbit. *Astronomy and Astrophysics*, **500**, 883-889. https://doi.org/10.1051/0004-6361/200911690

[5] Leahy, D. and Abdallah, M. (2014) HZ Her: Stellar Radius from X-Ray Eclipse Observations, Evolutionary State, and a New Distance. *The Astrophysical Journal*, **793**, Article No. 79. https://doi.org/10.1088/0004-637X/793/2/79

[6] Reynolds, A., Quaintrell, H., Still, M., *et al.* (1997) A New Mass Estimate for Hercules X-1. *Monthly Notices of the Royal Astronomical Society*, **288**, 43-52. https://doi.org/10.1093/mnras/288.1.43

[7] Arnason, R., Papei, H., Barmby, P., Bahramian, A. and Gorski, M. (2021) Distances to Galactic X-Ray Binaries with Gaia DR2. *Monthly Notices of the Royal Astronomical Society*, **502**, 5455-5470. https://doi.org/10.1093/mnras/stab345

[8] Leahy, D., Postma, J. and Chen, Y. (2020) AstroSat UVIT Observations of Her X-1. *The Astrophysical Journal*, **889**, Article No. 131. https://doi.org/10.3847/1538-4357/ab65f9

[9] Leahy, D (2003) Modelling the Extreme Ultraviolet Emission during the Low State of Hercules X-1. *Monthly Notices of the Royal Astronomical Society*, **342**, 446-452. https://doi.org/10.1046/j.1365-8711.2003.06542.x

[10] Jimenez-Garate, M., Hailey, C., den Herder, J., Zane, S. and Ramsay, G. (2002) High-Resolution X-Ray Spectroscopy of Hercules X-1 with the XMM-Newton Reflection Grating Spectrometer: CNO Element Abundance Measurements and Density Diagnostics of a Photoionized Plasma. *The Astrophysical Journal*, **578**, Article No. 391. https://doi.org/10.1086/342348

[11] Leahy, D. and Igna, C. (2011) The Light Curve of Hercules X-1 as Observed by the Rossi X-Ray Timing Explorer. *The Astrophysical Journal*, **736**, Article No. 74. https://doi.org/10.1088/0004-637X/736/1/74

[12] Petterson, J. (1975) Hercules X-1: A Neutron Star with a Twisted Accretion Disk? *The Astrophysical Journal Letters*, **201**, L61-L64. https://doi.org/10.1086/181942

[13] Wijers, R. and Pringle, J. (1999) Warped Accretion Discs and the Long Periods in X-Ray Binaries. *Monthly Notices of the Royal Astronomical Society*, **308**, 207-220. https://doi.org/10.1046/j.1365-8711.1999.02720.x

[14] Scott, D., Leahy, D. and Wilson, R. (2000) The 35 Day Evolution of the Hercules X-1 Pulse Profile: Evidence for a Resolved Inner Disk Occultation of the Neutron Star. *The Astrophysical Journal*, **539**, Article No. 392. https://doi.org/10.1086/309203

[15] Leahy, D. (2002) Modelling RXTE/ASM Observations of the 35-d Cycle in Her X-1. *Monthly Notices of the Royal Astronomical Society*, **334**, 847-854. https://doi.org/10.1046/j.1365-8711.2002.05547.x

[16] Leahy, D. and Wang, Y. (2020) Swift/BAT and RXTE/ASM Observations of the 35 Day X-Ray Cycle of Hercules X-1. *The Astrophysical Journal*, **902**, Article No. 146. https://doi.org/10.3847/1538-4357/abb611

[17] Scott, D. and Leahy, D. (1999) Rossi X-Ray Timing Explorer All-Sky Monitor Observations of the 35 Day Cycle of Hercules X-1. *The Astrophysical Journal*, **510**, Article No. 974. https://doi.org/10.1086/306631

[18] Leahy, D. and Igna, C. (2010) RXTE-Based 35 Day Cycle Turn-On Times for Hercules X-1. *The Astrophysical Journal*, **713**, 318-324. https://doi.org/10.1088/0004-637X/713/1/318

[19] Staubert, R., Klochkov, D., Vasco, D., *et al.* (2013) Variable Pulse Profiles of Hercules X-1 Repeating with the Same Irregular 35 d Clock as the Turn-Ons. *Astronomy and Astrophysics*, **550**, 110-118. https://doi.org/10.1051/0004-6361/201220316

[20] Inoue, H. (2019) Reproductions of Super-Orbital X-Ray Light-Curves with the Precessing Accretion Ring Model and Implications on Accretion Flows through Accretion Rings. *Publications of the Astronomical Society of Japan*, **71**, Article No. 36. https://doi.org/10.1093/pasj/psy152

[21] Vrtilek, S., Quaintrell, H., Boroson, B., *et al.* (2001) Multiwavelength Studies of Hercules X-1 during Short High and Anomalous Low States: On-Again, Off-Again. *The Astrophysical Journal*, **549**, 522-536. https://doi.org/10.1086/319071

[22] Parmar, A., Pietsch, W., McKechnie, S., *et al.* (1985) An Extended X-Ray Low State from Hercules X-1. *Nature*, **313**, 119-121. https://doi.org/10.1038/313119a0

[23] Leahy, D. and Dupuis, J. (2010) Extreme Ultraviolet Explorer Observations of Hercules X-1 over a 35 Day Cycle. *The Astrophysical Journal*, **715**, 897-901. https://doi.org/10.1088/0004-637X/715/2/897

[24] Igna, C. and Leahy, D. (2011) Light-Curve Dip Production through Accretion Stream-Accretion Disc Impact in the HZ Her/Her X-1 Binary Star System. *Monthly Notices of the Royal Astronomical Society*, **425**, 8-20. https://doi.org/10.1111/j.1365-2966.2012.21303.x

[25] Lubow, S. and Shu, F. (1975) Gas Dynamics of Semidetached Binaries. *The Astrophysical Journal*, **198**, 383-405. https://doi.org/10.1086/153614

[26] Becker, P. and Wolff, M. (2007) Thermal and Bulk Comptonization in Accretion-Powered X-Ray Pulsars. *The Astrophysical Journal*, **654**, 435-457. https://doi.org/10.1086/509108

[27] Leahy, D. (2004) An Accretion Column Model for the Accreting Pulsar Her X-1. *Monthly Notices of the Royal Astronomical Society*, **348**, 932-936. https://doi.org/10.1111/j.1365-2966.2004.07414.x

[28] Inoue, H. (2020) X-Ray Emissions from Magnetic Polar Regions of Neutron Stars. *Publications of the Astronomical Society of Japan*, **72**, Article No. 12. https://doi.org/10.1093/pasj/psz132

[29] Kondo, K., Dotani, T. and Inoue, H. (2021) Studies of Emission Regions of the X-Ray Pulsar Hercules X-1 with Pulse-Phase-Resolved Spectra Observed with Suzak. *Publications of the Astronomical Society of Japan*, **73**, 286-301. https://doi.org/10.1093/pasj/psaa120

[30] Vasco, D., Staubert, R., Klochkov, D., *et al.* (2013) Pulse Phase and Precession Phase Resolved Spectroscopy of Hercules X-1: Studying a Representative Main-On with RXTE. *Astronomy and Astrophysics*, **550**, A111. https://doi.org/10.1051/0004-6361/201220181

[31] Abdallah, M. and Leahy, D. (2015) Spectral Signature of Atmospheric Reflection in Hercules X-1/HZ Hercules during Low and Short High States. *Monthly Notices of the Royal Astronomical Society*, **453**, 4222-4231. https://doi.org/10.1093/mnras/stv1886

[32] Crosa, L. and Boynton, P. (1980) Periodic Mass Transfer in HER X-1/ HZ Her. *The Astrophysical Journal*, **235**, 999-1015. https://doi.org/10.1086/157705

[33] Choi, C., Nagase, F., Makino, F., Dotani, T. and Min, K. (1994) An X-Ray Spectroscopic Study of the Pre-Eclipse Dips of Hercules X-1. *The Astrophysical Journal*, **422**, 799-809. https://doi.org/10.1086/173772

[34] Leahy, D., Yoshida, A. and Matsuoka, M. (1994) Spectral Evolution during Pre-Eclipse Dips in Hercules X-1. *The Astrophysical Journal*, **434**, 341-348. https://doi.org/10.1086/174732

[35] Igna, C. and Leahy, D. (2011) Hercules X-1's Light-Curve Dips as Seen by the RXTE/PCA: A Study of the Entire 1996 February-2005 August Light Curve. *Monthly Notices of the Royal Astronomical Society*, **418**, 2283-2291. https://doi.org/10.1111/j.1365-2966.2011.19550.x

[36] Ushimaru, N., Tawara, Y., Koyama, K., *et al.* (1989) Energy Spectra and Pulse Profiles of Hercules X-1 at Pre-Eclipse Dips. *Publications of the Astronomical Society of Japan*, **41**, 441-452.

[37] Krimm, H., Holland, S., Corbet, R., *et al.* (2013) The Swift/BAT Hard X-Ray Transient Monitor. *The Astrophysical Journal Supplement*, **209**, Article No. 14. https://doi.org/10.1088/0067-0049/209/1/14

[38] Matsuoka, M., Kawasaki, K., Ueno, S., *et al.* (2009) The MAXI Mission on the ISS: Science and Instruments for Monitoring All-Sky X-Ray Images. *Publications of the Astronomical Society of Japan*, **61**, 999-1010. https://doi.org/10.1093/pasj/61.5.999

[39] Leahy, D. and Chen, Y. (2021) Results from AstroSat LAXPC Observations of Hercules X-1 (Her X-1). *Journal of Astrophysics and Astronomy*, **42**, Article No. 44. https://doi.org/10.1007/s12036-020-09676-1

[40] Singh, K., Tandon, S., Agrawal, P., *et al.* (2014) ASTROSAT Mission, Society of Pho-

to-Optical Instrumentation Engineers (SPIE) Conference Series, Article ID: 9144S. https://doi.org/10.1117/12.2062667

[41] Leahy, D. (2015) Hercules X-1: Using Eclipse to Measure the X-Ray Corona. *The Astrophysical Journal*, **800**, Article No. 32. https://doi.org/10.1088/0004-637X/800/1/32

[42] Jahoda, K., Swank, J., Giles, A., *et al.* (1996) In-Orbit Performance and Calibration of the Rossi X-Ray Timing Explorer (RXTE) Proportional Counter Array (PCA). *SPIE's* 1996 *International Symposium on Optical Science*, *Engineering*, *and Instrumentation*, Vol. 2808, 59-70. https://doi.org/10.1117/12.256034

[43] Gruber, D., Blanco, P., Heindl, W., *et al.* (1996) The High Energy X-Ray Timing Experiment on XTE. *Astronomy and Astrophysics Supplement*, **120**, 641-644.

[44] Remillard, R. and Levine, A. (1997) The RXTE All Sky Monitor: First Year of Performance, All-Sky X-Ray Observations in the Next Decade.

[45] Staubert, R., Klochkov, D., Fürst, F., *et al.* (2017) Inversion of the Decay of the Cyclotron Line Energy in Hercules X-1. *Astronomy and Astrophysics*, **606**, L13. https://doi.org/10.1051/0004-6361/201731927

[46] Leahy, D. and Wang, Y. (2021) The 35-Day Cycle of Hercules X-1 in Multiple Energy Bands from MAXI and Swift/BAT Monitoring. *Universe*, **7**, Article No. 160. https://doi.org/10.3390/universe7060160

[47] Leahy, D. and Abdallah, M. (2022) Spectral Evolution of Hercules X-1 over Main High State from RXTE/PCA Observations. *Journal of High Energy Physics*, *Gravitation and Cosmology*, **8**, 896-918. https://doi.org/10.4236/jhepgc.2022.84061

[48] Leahy, D. and Yoshida, A. (1995) Analysis of an Eclipse INGRESS during a High State of Hercules X-1. *Monthly Notices of the Royal Astronomical Society*, **276**, 607-613. https://doi.org/10.1093/mnras/276.2.607